RESEARCH ARTICLE

Microstrip-Ministered Proximity-Coupled Stacked Dual-Port Antenna for 6G Applications

SHAHANAWAZ KAMAL[ID] **AND PADMANAVA SEN**[ID] **, (Senior Member, IEEE)**
Barkhausen Institut, 01067 Dresden, Germany

Corresponding author: Shahanawaz Kamal (shahanawaz.kamal@barkhauseninstitut.org)

ABSTRACT A novel dual-port multiple-input−multiple-output (MIMO) antenna arrangement is introduced for attaining quasi-omnidirectional circular polarization (OCP) towards device-to-device (D2D) integrated sensing and communications (ISAC) deployment in sixth generation (6G) networks. The antenna architecture comprises of three dielectric laminates arranged one below/above the other with each substrate juxtaposed to its counterpart by the air cavity. The upper laminate encompasses solitary element frequency selective surface (FSS) etched on both fronts. Impedance matching transmission lines and partly reactive impedance surfaces (RIS) were printed on the top and bottom region of the middle substrate, respectively. The lower laminate features microstrip feed lines on the top side and semi ground planes on the bottom. The MIMO antenna was made up of two ports and fed through proximity coupling from the opposite ends of the middle substrate's top surface to resonate with a -10 dB impedance bandwidth (I-BW) of $\sim$35%. The partial RIS enabled >20 dB of isolation between the ports while the air cavities between the laminates contributed to achieve a realized gain of >7 dBi. The antenna occupies $1.2\lambda \times 1.2\lambda$ footprint and 0.1λ height at 12 GHz to exhibit quasi-OCP in the azimuth plane with axial ratio (AR) of <3 dB and efficiency of >90%. The envelope correlation coefficient (ECC), diversity gain, specific absorption rate (SAR), and power density (PD) at the band of interest were <0.1, $\sim$10 dB, <1.6 W/kg, and <10 W/m^2, respectively. The results of the Ansys HFSS simulations and the measurements taken within the anechoic chamber exhibited good agreement. In contrast to state-of-the-art quasi-OCP antennas operating in the 12 GHz spectrum, the novelty of the proposed MIMO antenna includes a straightforward and compact configuration that is integrated synergistically to provide reasonably high gain and efficiency values.

INDEX TERMS Antenna, circular polarization, frequency selective surface, high-efficiency, low-profile, miniature, metasurface, multiple-input–multiple-output, quasi-omnidirectional, reactive impedance surface.

I. INTRODUCTION

The dramatic rise of handheld gadget consumers has driven the need for a wireless access environment with lower latency, reduced power consumption, improved spectrum efficiency, and higher data rates over the preceding decade [1]. The 6G mobile standard is intended to transform consumer applications by enabling automatic administration and seamless communications across heterogeneous devices. D2D ISAC represents an innovation exhibiting potential for the 6G network to enable direct communication between two

The associate editor coordinating the review of this manuscript and approving it for publication was Davide Comite[ID].

adjacent consumer electronics without the requirement of a base station [2]. This ultimately renders feasibility for effective spectrum utilization and efficient dual-function operations.

Given the limited number of accessible frequency resources, spectrum sharing is an attractive strategy for the internet of things (IoT) [3]. Furthermore, wireless carriers are prone to utilizing the established infrastructures and protocols of mobile phone networks and deploying IoT within regulated telecom spectrum. Hence, ISAC systems are perpetually widening and amalgamating their frequency spectrum [4]. For instance, the 12 GHz spectrum have received substantial interest with the objective to investigate whether it could

potentially be employed for the high-speed wireless communication alongside various emerging applications. In addition, the constraints of the coverage provided by terrestrial networks have revived interest in satellite-based infrastructure for IoT [5]. The goal of IoT connectivity in isolated regions would be achieved with satellite-instituted setup and is anticipated to become increasingly vital in coming years.

The intensity of electromagnetic (EM) waves radiated from antennas usually diminishes as they extend further from their individual sources. A practical solution towards featuring high throughput and low latency networks represents high efficiency antennas. Employing miniaturized antennas is also a prerequisite imposed by contemporary electronics. Microstrip antennas realized on a printed circuit board are the incredibly prevalent owing to their compact geometry and straightforward circuit amalgamation potentials. In general, the substrates serve as vital for preserving the necessary radiation and antenna physical characteristics. Low-profile microstrip antennas, on the other hand, suffer from poor radiation efficiency and front-to-back ratio because the fields and images that the antenna emits in the far-field portion effectively cancel themselves out. Considerable effort has been devoted to developing metasurfaces to achieve an optimal front-to-back ratio [6]. However, the disadvantages of these techniques include their poor efficiency, bulky sizes, and difficult construction procedure. One method for achieving high efficiency antennas involve exercising substrates with low permittivity [7].

The MIMO antenna approach remain fundamental with their distinctive potential to simultaneously guarantee the transmission capacity and sensing accuracy [8]. However, the MIMO framework inevitably results in isolation problems, considerable hardware expenses, and substantial power utilization. Furthermore, quasi-omnidirectional antennas ought to be vital for IoT D2D ISAC [9], [10]. Then again, quasi-omnidirectionality induces phase inaccuracy and multiple paths wave reflection. CP antennas can ward off multiple paths fading from the ionosphere. As a result, quasi-OCP antennas form essential components of less precise navigation systems constructed on satellites. However, realizing a high radiation efficiency and a broad AR-BW are the main difficulties associated with developing a quasi-OCP antenna.

The primary objective of the present research intends to accomplish a quasi-OCP radiation pattern with an easy to fabricate MIMO antenna design for D2D ISAC in 6G IoT over satellite at 12 GHz. Particularly, we propose a dual-feed proximity-coupled MIMO antenna that consists of three dielectric slabs placed one on top of the other and separated by the air cavities. Two orthogonal EM waves with identical amplitude and a 90° phase difference were excited by the novel MIMO antenna configuration made up of metasurfaces. All the physical aspects that affect the impedance and radiation performance of the proposed MIMO antenna were extensively researched. To the best of the authors knowledge,
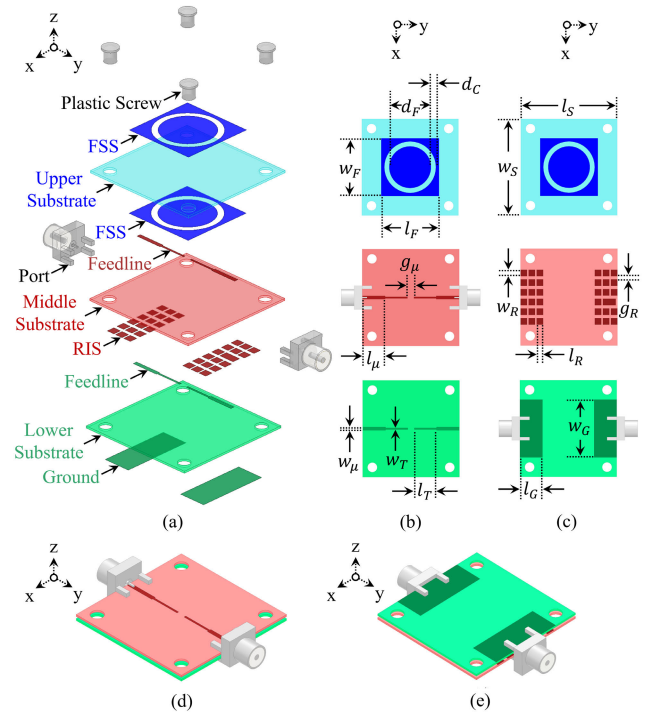

FIGURE 1. (a) Perspective, (b) top and (c) bottom configuration of the proposed MIMO antenna. Isometric projection of the port connections from the (d) top and (e) bottom sides.

TABLE 1. Antenna parameter values.

Parameter	Value (λ)	Description
l_S	1.2	substrate length
w_S	1.2	substrate width
l_G	0.3	ground length
w_G	0.7	ground width
l_μ	0.3	microstrip feed length
w_μ	0.04	microstrip feed width
l_T	0.3	transition of feedline length
w_T	0.002	transition of feedline width
l_R	0.08	RIS unit length
w_R	0.08	RIS unit width
l_F	0.7	FSS square unit length
w_F	0.7	FSS square unit width
d_F	0.3	FSS circular unit diameter
d_C	0.3	circular strip diameter
g_μ	0.08	gap between two microstrips
g_R	0.04	gap between two RIS units
t	0.02	thickness of each dielectric layer

the proposed quasi-OCP MIMO antenna exhibits the highest realized gain of >7 dBi in the literature whilst presenting a compact size of $1.2\lambda \times 1.2\lambda$ and low-profile of 0.1λ. Furthermore, the proposed MIMO antenna features a -10 dB I-BW of $\sim35\%$, AR of <3 dB, efficiency of $>90\%$, ECC of <0.1, diversity gain of ~10 dB, SAR of <1.6 W/kg, and PD of <10 W/m^2.

II. DESIGN AND CONFIGURATION
Fig. 1 illustrates the proposed MIMO antenna architecture that contains three dielectric substrates stacked one beneath the other, with the air cavities separating them all to constitute
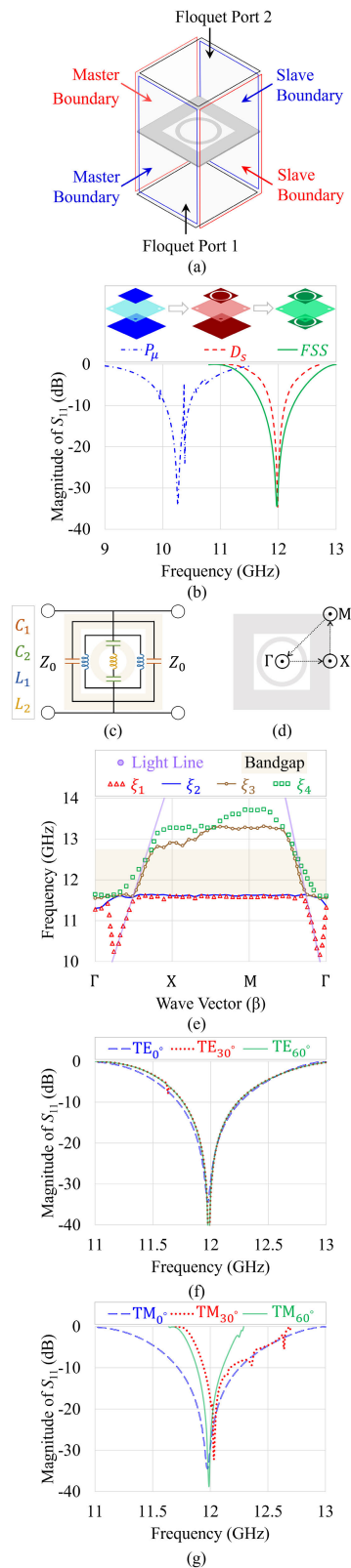
FIGURE 2. Proposed FSS: (a) Layout, (b) evolution, (c) equivalent circuit, (d) Brillouin region, (e) dispersion diagram, and $|S_{11}|$ of (f) TE and (g) TM waves.

and bottom surfaces of the middle substrate, respectively, were printed with impedance matching transmission lines and partly RIS. The lower laminate was equipped with microstrip feed lines on the top side and semi ground planes on the bottom side. The optimum set of parameters derived by Ansys HFSS simulations are documented in Table 1. The proposed MIMO antenna is systematically designed and analyzed whilst each component serves specific objectives to boost the overall performance. The rationale with respect to every preference is expressed in the subsections that follow.

A. FREQUENCY SELECTIVE SURFACE

Typically, the frequency filtering characteristics of FSS are comparable to those of the frequency filters used in conventional radio frequency systems [11], [12]. FSS features two primary applications. One exploits FSS reflectors for segregating feeds across different frequencies in antenna arrangements. The other implementation of FSS serves as antenna radomes that further regulate both transmitted and reflected EM waves. A single FSS ought to consist of a thin surface that is characterized by a conductive or resistive material arrangement on a surface that incorporates certain reinforcement, for instance a dielectric layer [13]. A FSS may also include surface-bonded components including transistors, inductors, diodes, and capacitors [14], [15]. These are frequently termed analog circuit architectures. FSS may be electrically isolated or might feature connection elements like vias between them [16]. FSS could be entirely passive, semi-active with biased diodes, active with amplification mechanisms, and the like [17], [18], and [19]. FSS might also include collections of entirely 3D items [20]. FSS may intentionally introduce loss as a component of a radar absorbent material, or it may be created to have zero loss [21]. The construction of FSS layouts employing several dielectric layers and/or FSS inserted within a composite is possible and frequently done [22]. Choosing a name for these structures while considering how they relate to antenna definitions, 2D or 3D metamaterials, dichroic surfaces, metasurfaces, and all that quickly becomes challenging. The majority of FSS applications presume that the patterns are periodic and are characterized by an infinitely repeating unit cell. However, this is not true in a number of fields with practical significance because the main goal usually represents to attain good filtering characteristics. Furthermore, many non-periodic FSS types have been studied in the past as examples of the same [23]. FSS are frequently constrained by the accuracy that they are capable of being etched and might be essential over huge sections of surface due to the engineering and financial challenges involved with them. This study aimed to enable high-performance filtering properties with a simple design that would be easy to manufacture. In particular, accomplishing the FSS features merely with the radiating patch and eliminating the requirement for additional layers.

the optimum antenna arrangement. The upper laminate was printed on both sides with single element FSS. The top

In the EM simulation environment, the master-slave boundary conditions with Floquet port were employed to evaluate the FSS layout, as shown in Fig. 2(a). The distance between the FSS and Floquet port was kept 0.5λ to ensure that all evanescent modes diminish before reaching the unit cell. The FSS design was investigated by considering three distinct cases to furnish a resonance in the 12 GHz spectrum, as shown in Fig. 2(b). At the outset, a square microstrip patch (P_μ) was simulated and its dimensions were approximated using the formulas based on the resonant frequency (f_r) stated in [24]. The square patch established a resonance between 10 GHz and 11 GHz. Hence, fine tweaking was initiated to ensure that the structure operates exclusively in the desired spectrum of interest. Particularly, in the second stage, a FSS that serves as a filter for free-space signals with frequency-dependent EM propagation characteristics was taken into account. Furthermore, the case was viable to block beyond the band information while allowing signals within the preferred spectrum to propagate. The features of a FSS were yielded by adding a supplementary part to the square patch. The accumulation was engineered taking into consideration the fundamental principle which stipulates that when an EM field illuminates a strip dipole (D_s) component and the dimension of the dipole count as a multiple of 0.5λ, the dipole will produce resonance and re-emit the electrical energy. A circular-loop unit composed of a pair of half-circular-loops that function as strip dipoles was explored to accomplish a resonance in the prerequisite spectrum of 12 GHz. An I-BW of ~2% was ascertained. Finally, the third case (FSS) was geared toward boosting the I-BW. This was accomplished by transforming the bottom side of the FSS based on the top side that has been discussed in phase two. The transition from the second to the third stage resulted in an I-BW of ~5%. Fig. 2(c) demonstrates the equivalent circuit model of the proposed FSS that includes an LC circuit with the letters C and L standing for, respectively, the inter-element spacing and the conducting elements. This model produced a $|S_{11}|$ response that was exactly like the one depicted in the FSS case highlighted in green in Fig. 2(b). The resonant frequency equation mentioned in [24] can be utilized to determine the values of lumped elements.

The eigenmode simulation was carried out whilst considering the Brillouin domain to further evaluate the FSS property, identify the permissible propagation modes, and determine the operational range of the proposed unit cell [25]. The Γ point represents the focal point of the Brillouin region, whereas the M and X points correspond to, respectively, the midpoints of an edge and a face, as illustrated in Fig. 2(d). The relationship between the wave vector and these points is expressed in [26]. Fig. 2(e) depicts the dispersion diagram of the proposed FSS with different propagation modes (ξ) activated. The EM bandgap region became apparent in the 12 GHz spectrum. Given the presence of symmetric FSS on both sides of the dielectric substrate, the first two modes produced comparable response curves.
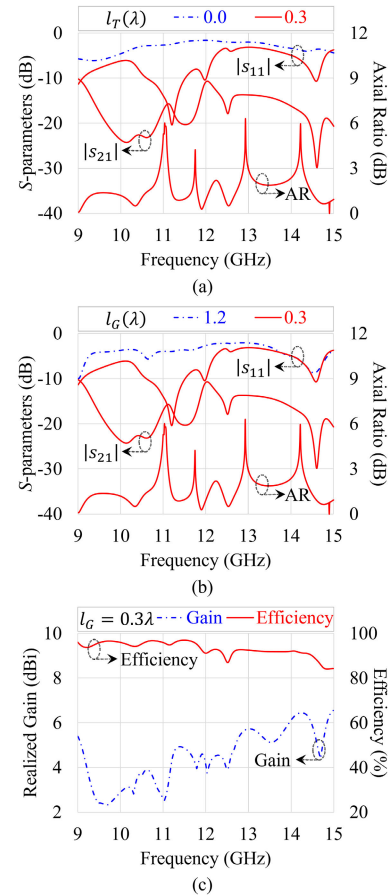

FIGURE 3. Impact of the (a) feedline transition and (b) ground plane dimension on $|S_{11}|$, $|S_{21}|$ and AR. (c) Realized gain and efficiency curves yielded from the antenna based on semi ground plane.

Finally, the effect of changing the angle of incidence (0°, 30°, and 60°) for TE and TM polarized waves was investigated, as demonstrated in Figs. 2(f) and 2(g), respectively. All modes achieved the anticipated resonance at 12 GHz, thus validating the FSS property of the proposed design.

B. FEED ELEMENT AND GROUND PLANE

With the aim to advance on to the succeeding phase, a MIMO setup based on the FSS design identified in the preceding subsection was studied. In this instance, procuring a broad I-BW in the 12 GHz spectrum remained the ultimate objective. A 0.25λ transformer was respected as the feed element to diminish the amount of energy reflected whilst the transmission line links to the load. Two feed elements were encompassed in the MIMO antenna system, and they were positioned at the opposite ends. A dielectric slab whose extents matched the dimensions of the standard connectors served as a platform for the feed elements. The proximity-coupled feeding approach was applied to produce a reasonable I-BW. The feed line dimensions are typically regarded as among the vital parts in a proximity-coupled antenna. This constitutes mainly because the geometry of
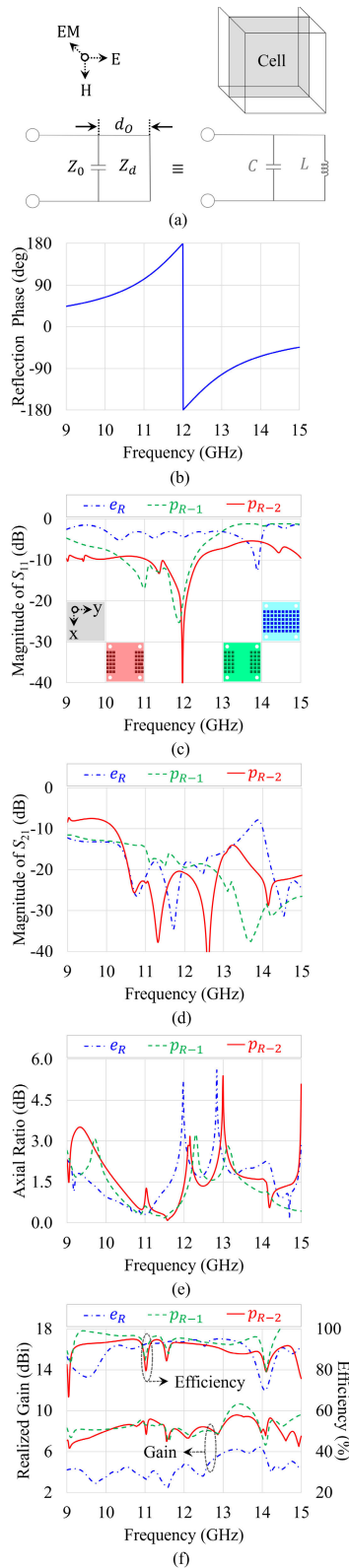
FIGURE 4. Proposed RIS: (a) model and equivalent circuit, (b) reflection phase, (c) |S_{11}|, (d) |S_{21}|, (e) AR, (f) realized gain and efficiency.

the microstrip affects the framework's resonance frequency, thereby affecting the quantity of intended forward EM radiation.

Two distinct feed element scenarios were investigated. In the initial instance, both feed length transitions (l_T) were constrained to the square patch's perimeter. In the second case, both feed length transitions were increased to reach the circular patch. Fig. 3(a) render it apparent that the feed components are extended until the circular patch produced a resonance near 12 GHz. The subject should be noted that the efficacy was realized by incorporating semi ground planes, which was the focus of a similar investigation. Fig. 3(b) shows the results of the study on the impact of full and semi ground planes (l_G). The increased separation between the conducting portions remains accountable for attaining an I-BW of ∼8% with >15 dB isolation response. Yet, their responses to AR of <6 dB weren't perceived to be optimum. Fig. 3(c) discloses that an efficiency of ∼95% may also be achieved at the cost of the low realized gain value of ⩽4 dBi in the operating frequency band.

C. REACTIVE IMPEDANCE SURFACE

Traditional microstrip patch antennas on metal-backed layers often have a narrow bandwidth and low efficiency [24]. These issues arise because the EM waves from the antenna image are susceptible to cancellation from the antenna current. Furthermore, it is challenging to match the antenna input impedance or would only be successful across a limited bandwidth. On the quest to overcome these issues, impedance surfaces offer the appropriate front-to-back EM radiation ratio and permit the insertion of concurrent electric currents in their vicinity [27]. However, their input resistance expands, though, making it trickier to match the reactive portion. Furthermore, the conductor and dielectric losses of perfect magnetic conductors turn lossy and capture the antenna near-field energy, which eventually has a negative impact on the antenna efficiency. As a result, the antenna substrate constitutes a crucial part that influences the input impedance, and mutual coupling between the antenna and its image. A potential remedy for these issues constitutes the integration of periodic microstrip patches on the surface of a metal-backed dielectric substrate, typically referred as RIS [28], [29], [30]. Perfect magnetic and electrical conductors exhibit reflection phases of 180° and 0°, respectively. The contrary, RIS represents an entirely reactive surface by establishing arbitrary reflection phases between −180° and +180°. Hence, RIS generalizes both a perfect magnetic and electric conductor. In this work, the primary goal was to deploy RIS to sinusoidally distribute the image current in a bid to drastically diminish the interaction amongst the source and its image. In essence, to shift a capacitively or inductively loaded antenna resonance to a lower frequency and enhance the impedance matching. This is typically attainable whilst the surface impedance of RIS is appropriately considered. For instance, the surface impedance η of RIS is designated as jv [31].

A metasurface layer was added to the MIMO antenna design in order to improve the I-BW and isolation response

while retaining the compact shape. This layer encompassed the feed elements with dimensions derived from subsection *B* on the top side and squared metal segments of RIS on the bottom. Theoretically, a unit RIS cell operates identical to a shunt capacitor fixed at an offset distance (d_O) from a short circuited microstrip, as shown in Fig. 4(a). A parallel *LC* circuit ought to be employed to demonstrate the aforementioned. The unit cell simulation result stated in Fig. 4(b) indicates that the RIS exhibits capacitive, inductive, and open-circuit behavior below, at, and above the frequency of their resonance, respectively. A distance of one wavelength was maintained as the upper limit for the periodicity of RIS unit cells. This enabled the capacity to recognize differences between the RIS and FSS.

Initially, the effects of RIS on the entire plane (e_R) was investigated, as indicated in Fig. 4(c)−(f). A shift in the resonance frequency to 14 GHz with AR of <3 dB was accomplished. Additionally, the metal RIS parts present near FSS increased the mutual coupling. Hence, an alternative instance of partial RIS (p_{R-1}) was studied wherein the RIS was split into two halves with dimensions equal to the size of the ground plane that was established in subsection *B*. The antenna yielded peak resonance at 11.9 GHz with notable isolation enhancement relative to the prior case, as displayed in Fig. 4(c)−(d). Furthermore, another case of partial RIS (p_{R-2}) was investigated in which two RIS units near a feed element were merged to attain peak resonance at 12 GHz whilst taking into account the basic hypothesis of antennas. Subsequently, a wide I-BW of >30% and reasonable isolation of >20 dB was established in the 12 GHz spectrum, as displayed in Fig. 4(c)−(d). These improvements were potentially linked to the RIS ability to store magnetic field energy, that impacts the FSS total inductance thereby making up for the electric energy stored in proximity to the antenna. Furthermore, AR of <3 dB was yielded with a modest enhancement in the realized gain of >7 dBi and efficiency of >90%, as indicated in Fig. 4(e)−(f). Note that these advancements are attributable to the dielectric layers that are detailed in the next subsection.

D. DIELECTRIC LAYER

To accomplish notable gain and efficiency values, the dielectric layer topology was examined. The dielectric layers with low relative permittivity were introduced to avoid signal loss. Particularly, the air ($\epsilon_r = 1$) cavities were interpolated to mitigate against surface waves excitation. Additionally, the stacked arrangement of high and low dielectrics provided a reduction in the antenna's effective relative permittivity to electrical resistance. Descriptively, the air cavity between the two dielectric substrates may be regarded as a cavity area enveloped by magnetic boundaries on the sides, and electric boundaries on the top and bottom due to the presence of conductors. A consideration may also be paid to the bottom conductor operating as the top cavity's ground, thereby mitigating the mutual coupling effect driven through the surface waves produced by the dielectric laminates.
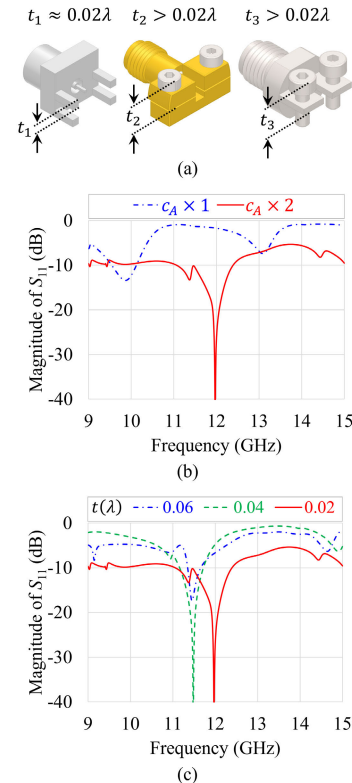
FIGURE 5. (a) Connectors (left to right): SMA, Rosenberger, and SV Microwave. $|S_{11}|$ and $|S_{21}|$ responses corresponding to variations in the (b) assembly and (c) thickness of dielectric layers.

The dielectric layer studies were based on the fabrication/assembly constraints as developing a straightforward design constitutes an objective. Furthermore, it was necessary to opt for an economical option. Hence, the type of connector to be employed was explored. Despite the wide variety of connector choices available for 12 GHz operation, three types including SubMiniature Version A (SMA) BU-1420701851, Rosenberger 02K243-40ME3, and Amphenol SV Microwave 3321-60059 are frequently used for edge feeding, as shown in Fig. 5(a). These options are advantageous in view of the performance and/or financial advantages they offer. However, in this work, the SMA connector was elected as the appropriate solution because of the following three reasons. Primarily, the mechanical stability represented a challenge since the proposed antenna was fed in a unique fashion in contrast to standard antennas. Secondly, the air cavity thickness between the middle and top substrates must be ≈0.02λ for SMA and >0.02λ for other connectors as the portion beside the feed pin of the connector would obstruct the positioning of the top substrate, forcing the board area to be trimmed. Finally, the SMA connector is relatively inexpensive. Nevertheless, the air cavity thickness between the middle and lower substrates must be ⩽0.02λ because the feed pin of SMA connector was intended to be soldered to the top side of the middle substrate, and their ground pin to the bottom side of the lower substrate.

Investigating two distinct examples led to the optimal arrangement being identified. In the first instance ($c_A \times 1$),
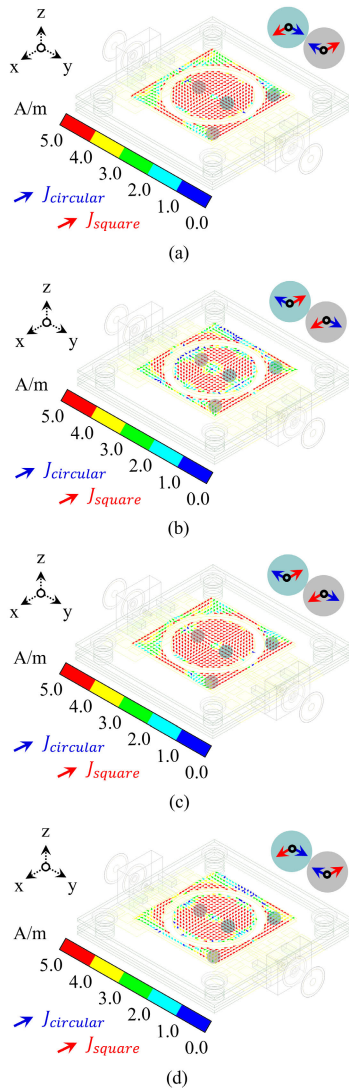
FIGURE 6. Simulated results of the proposed MIMO antenna at 12 GHz: CP mechanism for (a) $\phi = 0°$, (b) $\phi = 90°$, (c) $\phi = 180°$ and (d) $\phi = 270°$.

only the upper and middle dielectric slabs were separated by an air cavity of $t = 0.02\lambda$, whereas in the second case ($c_A \times 2$), the air cavities of $t = 0.02\lambda$ were introduced between all dielectric substrate layers. The second investigation yielded the desired resonance at 12 GHz with relatively broad I-BW, as depicted in Fig. 5(b). To ascertain the fabrication tolerance, three different estimates ($t = 0.06\lambda$, $t = 0.04\lambda$, and $t = 0.02\lambda$) of the air cavity thickness between the middle and the upper substrates were examined. Fig. 5(c) represent their frequency response curves. It was concluded that the EM radiation was appropriately coupled with the FSS by the fringing fields for $t = 0.02\lambda$. Note that $c_A \times 2$ and $t = 0.02\lambda$ are the same cases.

III. OPERATING PRINCIPLE

The current distributions at 12 GHz have been explored and are discussed in the forthcoming subsections to assess the operating principle of the proposed MIMO antenna. The
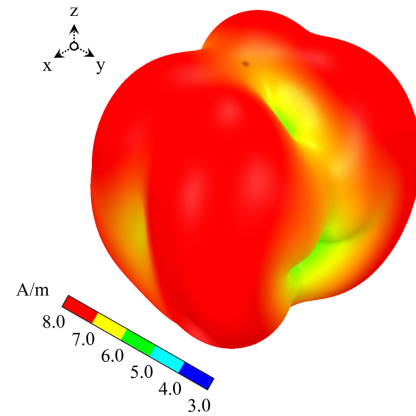
FIGURE 7. Quasi-omnidirectional radiation pattern of the proposed MIMO antenna at 12 GHz.

subject issue is introduced by taking into account current directions at various phase angles to describe the CP behavior. Subsequently, the surface current distribution for analyzing the effects of isolation is presented. Furthermore, SAR and PD analysis are detailed to illustrate the amount of EM radiation that human tissue potentially absorb. Finally, the impact of human hand on the antenna radiation pattern is evaluated.

A. QUASI-OMNIDIRECTIONAL RADIATION PATTERN AND CIRCULAR POLARIZATION

Fundamentally, two orthogonal constituents exhibiting a 90° phase deviation are essential for establishing the CP EM radiation. The CP mechanism was considerably stimulated by the FSS architecture. Examining the trajectory of the current flow shown in Fig. 6(a)−(d) is intended to demonstrate the conclusion. The highlighted currents in the circular patch ($J_{circular}$) of the FSS were produced respectively in the directions of $+y$ and $-y$ at 0°, $-y$ and $+y$ at 90°, $-y$ and $+y$ at 180°, and $+y$ and $-y$ at 270°. The focused currents, on the other hand, formed respectively in the square part (J_{square}) of the FSS in the directions of $+x$ and $-x$ at 0°, $-x$ and $+x$ at 90°, $-x$ and $+x$ at 180°, and $+x$ and $-x$ at 270°. The stripped circular-loop unit permitted to sabotage the passage of the current, which ultimately resulted in the formation of principal currents flowing in multiple directions. Additionally, a 0.25λ difference was kept between the lengths of the two feed lines to have the CP EM radiation enabled. Fig. 7 shows the 3D radiation pattern of the proposed MIMO antenna, which indicates that a quasi-omnidirectional response has been established. The air cavity between the substrates was primarily responsible for the unroundness of the radiation pattern. However, the feasibility of quasi-omnidirectional antennas have been proved for mobile communications in the past [32], [33], [34], [35].

B. MUTUAL COUPLING

This subsection provides an expanded overview of isolation effects, even though the approach to increase port isolation

has been covered by showing the transmission coefficient response in section II. Two distinct scenarios in particular with RIS and without RIS were examined, as confirmed in Fig. 8(a)−(b). In the cases of without RIS, the surface currents from ports 1 to 2 were coupled. Alternatively, the RIS based arrangement that has been proposed contributed to limit the current transfer from one port to the other.

C. BIOLOGICAL IMPACTS

The prevalence of wireless devices has dramatically expanded, increasing exposure to the EM fields, which are known to have a number of negative impacts on human health. As a result, SAR was analyzed using the subsequent formulas as estimates [36].

$$SAR = \sigma \frac{E^2}{\rho} \qquad (1)$$

$$\overrightarrow{E(r)} = \frac{1}{j\omega\mu\epsilon} \{k^2 \overrightarrow{A} + \nabla(\nabla \overrightarrow{A})\} \qquad (2)$$

where, σ expresses the electrical conductivity of the human tissue in S/m, E denotes the root mean square of the electric field strength in V/m, ρ signifies the mass density of the biological tissue in kg/mm^3, ω stands for the angular frequency, μ remains the permeability of the tissue, k exemplifies for the propagation constant, $\overrightarrow{A}$ represents the magnetic vector potential, and ∇ symbolizes the differential power. The terms $k^2 \overrightarrow{A}$ and $\nabla (\nabla \overrightarrow{A})$ signifies the dominant part of electric far-field and near-field, respectively [37].

A human hand phantom was used to assess the SAR characteristics of the proposed MIMO antenna, as illustrated in Fig. 9(a). The result shows that the maximum SAR is within the safety limits of <1.6 W/kg [38].

PD represents another safety assessment metric that is typically evaluated for antennas operating at higher frequencies, particularly >10 GHz [39]. Two physical quantities—an electric field ($\overrightarrow{E}$) and a magnetic field ($\overrightarrow{H}$)—are required to compute PD. The real term of the Poynting vector ($\overrightarrow{S}$) derived from the cross product of $\overrightarrow{E}$ and complex conjugation of $\overrightarrow{H}$ represents the actual consumption power, as stated in the following equation [40], [41].

$$\langle \overrightarrow{S} \rangle = Re \left(\frac{1}{2} \overrightarrow{E} \times \overrightarrow{H^*} \right) \qquad (3)$$

where, $\langle \overrightarrow{S} \rangle$ refers to the localized PD determined by the peak value of every spatial location on the mesh grids.

The spatially averaged or total PD (μ_D) on an assessed area (A) can be obtained from the localized PD $\langle \overrightarrow{S} \rangle$, as expressed in the succeeding formula [40], [41].

$$\mu_D = \frac{1}{A} \int_A \langle \overrightarrow{S} \rangle \cdot ds = \frac{1}{2A} \int_A | Re(\overrightarrow{E} \times \overrightarrow{H^*}) | \cdot ds \qquad (4)$$

Fig. 9(b) presents the PD contour map of the proposed MIMO antenna at 12 GHz. The maximum PD value is well under the safety limits of <10 W/m^2 [39].
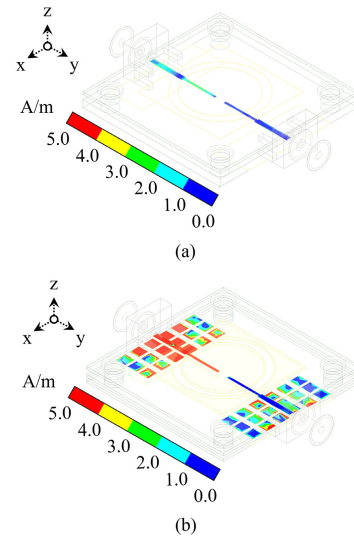

FIGURE 8. Investigation of the mutual coupling effect with the surface current produced by the MIMO antenna: (a) without RIS and (b) with RIS.

In due respect to the applications that favor actual SAR/PD measurements, it is advisable to consider SAR/PD measurements before practical implementation of the proposed antenna. This is important because the SAR/PD measurement facility at the affiliation of authors is now under construction, making these measurements impossible.

The impact of human hand on proposed MIMO antenna performance has been investigated. In the simulation setup, the SMA connector models were not included; instead, lumped ports were utilized to excite the two ports of the antenna. Fig. 9(c) demonstrate the three-dimensional (3-D) radiation pattern of the proposed MIMO antenna at 12 GHz. Quasi-omnidirectional radiation pattern with reasonable gain response was established in contrast to the simulation without the human hand. Particularly, a slight drop in the antenna gain was noticed near the human hand.

IV. EXPERIMENTAL RESULTS

To validate the simulation results, two MIMO antennas based on the $RO4003C^{TM}$ and $RO4350B^{TM}$ were developed by employing, respectively, the LPKF Laser & Electronics machine and standard photo-lithography approach. The photographs of the fabricated MIMO antenna prototypes are displayed in Fig. 10. The MIMO antenna measurements performed in the anechoic chamber at the Barkhausen Institut, Germany are described in the subsections that follow. A 50Ω termination resistance was deployed whilst measuring the radiation parameters. The measured (m_x) and simulated (s_x) results, with $x = [1, 2]$, of the constructed antenna prototypes demonstrated a good agreement between majority of the sets of observations. Owing to the nearly symmetric design of the proposed antenna, comparable results were seen when one port of the antenna was excited, and the other port was either 50Ω terminated or excited. However,
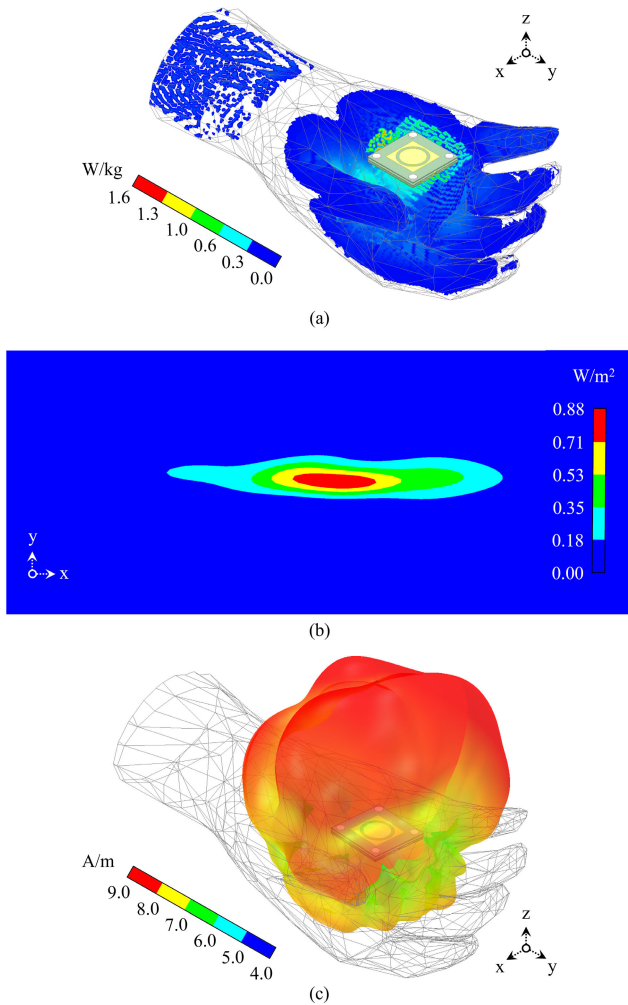
FIGURE 9. Analysis of (a) SAR, (b) PD and (c) 3-D radiation pattern on the human hand at 12 GHz with the proposed MIMO antenna.

FIGURE 10. Fabricated MIMO antennas.

there were fluctuations in the measured radiation patterns. The main reasons for the degradation might be due to the imperfections in fabrication process, connector tolerances, termination resistance, undesired EM radiations from the feed cable, and misalignment. Furthermore, the responses of the two antennas based on $RO4003C^{TM}$ and $RO4350B^{TM}$
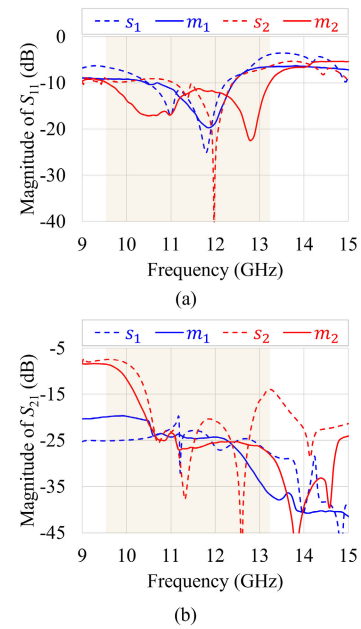

FIGURE 11. Simulated and measured (a) $|S_{11}|$ and (b) $|S_{21}|$ of the proposed antennas.

differed in some situations, which can be attributed to the varied dielectric substrate properties.

A. ANTENNA PERFORMANCE

The measured -10 dB I-BW for the $RO4003C^{TM}$ (m_1) was $>25\%$, and for the $RO4350B^{TM}$ (m_2) was $\sim35\%$, as depicted in Fig. 11(a). The measured mutual coupling in the operating band remained below -20 dB for both the fabricated prototypes, as shown in Fig. 11(b).

Fig. 12 shows the simulated and measured radiation patterns of the proposed MIMO antenna at 12 GHz. The radiation performance measurements were repeated for two distinct antenna orientations where the antenna under test was set up vertically and horizontally in the port direction. In the azimuth plane, the radiation pattern resembles quasi-omnidirectional.

The gain difference between the two orientations equated the antenna AR of <3 dB and denoted the CP behavior, as demonstrated in Fig. 13(a). The realized gain was >7 dBi in the operational frequency band, as portrayed in Fig. 13(b). Finally, both the prototypes produced an efficiency of more than 90%, as shown in Fig. 13(c), with the efficiency measurement relying on an estimation of the antenna directivity from the measured radiation patterns in the two fundamental planes.

B. MIMO PERFORMANCE

Fig. 14(a) and 14(b) shows, respectively, the ECC and diversity gain of the proposed MIMO antennas. Both the prototypes exhibited ECC of <0.1 and diversity gain of ~10 dB over their operational spectrum, thus confirming effective MIMO performance. The following formulations
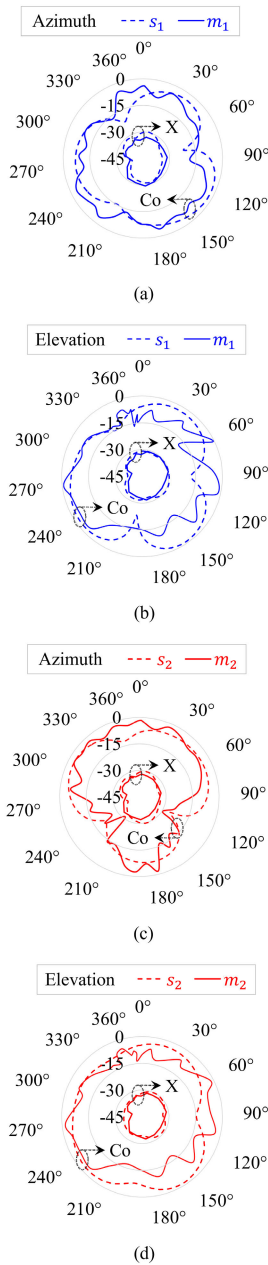
FIGURE 12. Simulated and measured right (Co) and left (X) hand radiation patterns of the proposed antennas at 12 GHz. (a) Azimuth and (b) elevation planes for $RO4003C^{TM}$. (c) Azimuth and (d) elevation planes for $RO4350B^{TM}$.
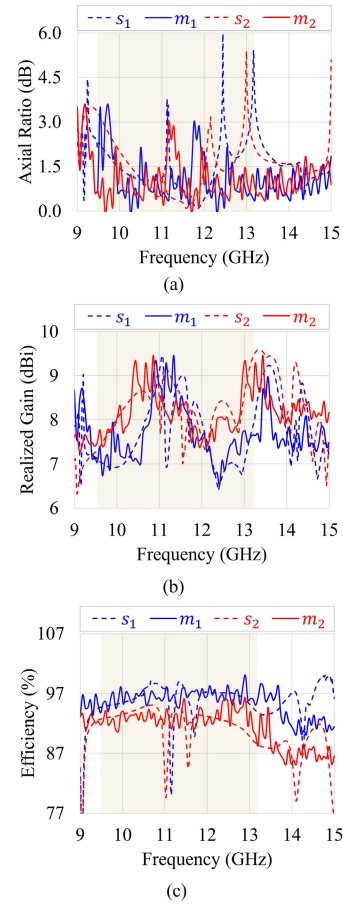
were used to approximate the ECC and diversity gain [42].

$$\text{ECC} = \frac{\mid \int \int_0^{4\pi} [\overrightarrow{F_i}(\theta, \phi) \times \overrightarrow{F_j}(\theta, \phi) d\Omega] \mid^2}{\int \int_0^{4\pi} \mid \overrightarrow{F_i}(\theta, \phi) \mid^2 d\Omega \int \int_0^{4\pi} \mid \overrightarrow{F_j}(\theta, \phi) \mid^2 d\Omega} \tag{5}$$

$$\text{Diversity Gain} = 10\sqrt{1 - (\text{ECC})^2} \tag{6}$$

where, $\overrightarrow{F_i}(\theta, \phi)$ and $\overrightarrow{F_j}(\theta, \phi)$ indicates, respectively, the ith and j^{th} elements of the antenna's radiation patterns.

The proposed MIMO antenna design and respective configuration have a good fabrication tolerance, owing to the

FIGURE 13. Simulated and measured (a) AR, (b) realized gain and (c) efficiency of the proposed antennas.
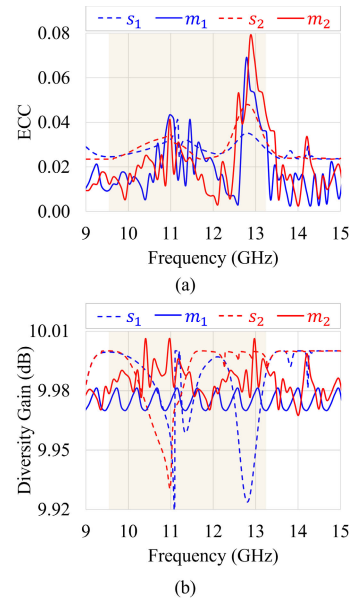
FIGURE 14. Simulated and measured (a) ECC and (b) diversity gain of the proposed antennas.

experimental results. Therefore, based on the availability of the dielectric material, mass production would be feasible. Furthermore, even if the air cavity thickness deviates

TABLE 2. Performance evaluation of contemporary antennas in contrast to the proposed MIMO antenna.

Antenna configuration archetype	f_r (GHz)	I-BW (%)	$|S_{21}|$ (dB)	AR (dB)	Gain (dBi)	Efficiency (%)	Footprint (λ^2)	Profile (λ)	Reference
Conformal metasurface	10.0	~20	—	<3	~2	>90	262	0.20	[43]
Anisotropic metasurface	13.0	~4	—	<3	—	>90	6.0 × 6.0	0.07	[44]
EM band gap metasurface	11.5	~6	<−20	<3	~4	~80	1.9 × 2.1	0.07	[45]
Dual feedlines with defected ground	12.0	~72	<−20	>3	~6	—	2.3 × 2.6	0.03	[46]
Monopole with defected ground	11.9	~5	—	<3	<4	<90	0.8 × 0.8	0.07	[47]
FSS and RIS integrated metasurface	12.0	~35	<−20	<3	>7	>90	1.2 × 1.2	0.10	This work

somewhat from the ideal value, the expected responses in terms of various antenna characteristics shall nevertheless be established.

V. BENCHMARKING

A number of FSS-based antennas have been reported in the literature for operation in the 12 GHz spectrum [48], [49], [50]. However, CP is vital for D2D ISAC. Hence, the proposed MIMO antenna has been compared with contemporary antennas in Table 2 in terms of the antenna configuration employed for generating CP waves, I-BW, isolation, AR, realized gain, efficiency, radiator size, and overall height. The resonant frequencies of the antennas are also listed in the table for an equitable comparison. Note that the strategies described in the literature may partially correspond to the version that is being presented in regards to the context for operation and the performance metrics. The cited antennas substantially enhance the performance of the entire system. These investigations yet contain a number of limitations that have been addressed in this article. The novelty and significance of the proposed antenna are mentioned in the subsequent points.

1) The proposed MIMO antenna features a straightforward metasurface for producing quasi-OCP waves. Particularly, realizing the shape and assembly of the metasurfaces is simple. The conformal linear-to-circular polarization conversion metasurface described in [43] has a difficult fabrication process and necessitates a substantial area. An anisotropic metasurface polarization converter [44] and an EM bandgap metasurface [45] have simple antenna geometries, but they require a larger area in comparison to the proposed MIMO antenna to enable CP waves.

2) The proposed antenna exhibits high efficiency and a wide I-BW. The downsizing, AR, and gain responses are substantially superior with the proposed antenna despite experiencing a lower I-BW when compared to the antenna made up of dual feedlines and a defective ground [46].

3) Compact geometry characterizes the proposed MIMO antenna. The I-BW and gain response of the monopole antenna coupled with defective ground [47] are poor notwithstanding its reasonably small architecture.

4) The most important contribution of the proposed MIMO antenna design entails the fact that it has the highest gain for all the comparison set and delivers superior overall performance in a compact package.

VI. CONCLUSION

The principal objective of establishing a quasi-OCP radiation pattern at 12 GHz by deploying a simple MIMO antenna arrangement has been accomplished. Three dielectric slabs were stacked one on top/below of the other and separated by air cavities to form the MIMO antenna framework. The proximity-coupled feeding method was adopted to excite the MIMO antenna featuring two ports. CP EM waves were stimulated by metasurfaces. Every physical factor that potentially impacted the way the MIMO antenna handled radiation and impedance performance was studied. The layout exhibited a reasonable I-BW, high efficiency, excellent MIMO performance, and a SAR/PD that is within acceptable limits. The computational and experimental proof were utilized to confirm the performance of the antenna and MIMO. If solely the proposed FSS architecture is considered for compact systems, relatively large size seems to be a limitation. However, the drawback is justified because the overall layout attains good filtering properties and significant improvements in other antenna characteristics. The proposed MIMO antenna therefore represents a suitable candidate for D2D ISAC in 6G networks, specifically IoT over satellite applications. Finally, this study constitutes a building block of a massive MIMO array.

REFERENCES

[1] H. Tataria, M. Shafi, A. F. Molisch, M. Dohler, H. Sjöland, and F. Tufvesson, "6G wireless systems: Vision, requirements, challenges, insights, and opportunities," *Proc. IEEE*, vol. 109, no. 7, pp. 1166–1199, Jul. 2021.

[2] S. Zhang, J. Liu, H. Guo, M. Qi, and N. Kato, "Envisioning device-to-device communications in 6G," *IEEE Netw.*, vol. 34, no. 3, pp. 86–91, May 2020.

[3] D. C. Nguyen, M. Ding, P. N. Pathirana, A. Seneviratne, J. Li, D. Niyato, O. Dobre, and H. V. Poor, "6G Internet of Things: A comprehensive survey," *IEEE Internet Things J.*, vol. 9, no. 1, pp. 359–383, Jan. 2022.

[4] D. K. Pin Tan, J. He, Y. Li, A. Bayesteh, Y. Chen, P. Zhu, and W. Tong, "Integrated sensing and communication in 6G: Motivations, use cases, requirements, challenges and future directions," in *Proc. 1st IEEE Int. Online Symp. Joint Commun. Sens.*, Feb. 2021, pp. 1–6.

[5] M. Centenaro, C. E. Costa, F. Granelli, C. Sacchi, and L. Vangelista, "A survey on technologies, standards and open challenges in satellite IoT," *IEEE Commun. Surveys Tuts.*, vol. 23, no. 3, pp. 1693–1720, 3rd Quart., 2021.

[6] O. A. Saraereh, "Design and performance evaluation of OAM-antennas: A comparative review," *IEEE Access*, vol. 11, pp. 27992–28013, 2023.

[7] M. Mohammadi Shirkolaei, "Wideband linear microstrip array antenna with high efficiency and low side lobe level," *Int. J. RF Microw. Comput.-Aided Eng.*, vol. 30, no. 11, Nov. 2020, Art. no. e22412.

[8] S. Kamal, M. F. Ain, U. Ullah, and M. F. M. Omar, "Enabling MIMO antenna miniaturization and wide circular polarization coverage by amalgamation of a dielectric strip between meandered traces and slotted ground," *IEEE Antennas Wireless Propag. Lett.*, vol. 21, no. 9, pp. 1901–1905, Sep. 2022.

[9] B. Xiao, H. Wong, D. Wu, and K. L. Yeung, "Design of small multiband full-screen smartwatch antenna for IoT applications," *IEEE Internet Things J.*, vol. 8, no. 24, pp. 17724–17733, Dec. 2021.

[10] S. Kamal, M. F. B. Ain, U. Ullah, A. S. B. Mohammed, R. Hussin, M. F. B. M. Omar, F. Najmi, Z. A. Ahmad, M. F. A. Rahman, M. N. Mahmud, M. Othman, and J. J. Mohamed, "A low-profile quasi-loop magneto-electric dipole antenna featuring a wide bandwidth and circular polarization for 5G mmWave device-to-device communication," *J. Electromagn. Eng. Sci.*, vol. 22, no. 4, pp. 459–471, Jul. 2022.

[11] T.-K. Wu, "Frequency selective surfaces," in *Encyclopedia of RF and Microwave Engineering*. Hoboken, NJ, USA: Wiley, 1995.

[12] J. A. Mackay, B. Sanz-Izquierdo, and E. A. Parker, "Evolution of frequency selective surfaces," *Forum Electromagn. Res. Methods Appl. Technol.*, vol. 2, no. 8, pp. 1–7, Mar./Apr. 2014.

[13] E. Rodes, M. Diblanc, E. Arnaud, T. Monediere, and B. Jecko, "Dual-band EBG resonator antenna using a single-layer FSS," *IEEE Antennas Wireless Propag. Lett.*, vol. 6, pp. 368–371, 2007.

[14] R. Dickie, R. Cahill, H. Gamble, V. Fusco, M. Henry, M. Oldfield, P. Huggard, P. Howard, N. Grant, Y. Munro, and P. de Maagt, "Submillimeter wave frequency selective surface with polarization independent spectral responses," *IEEE Trans. Antennas Propag.*, vol. 57, no. 7, pp. 1985–1994, Jul. 2009.

[15] R. Anwar, L. Mao, and H. Ning, "Frequency selective surfaces: A review," *Appl. Sci.*, vol. 8, no. 9, p. 1689, Sep. 2018.

[16] D. Li, T.-W. Li, E.-P. Li, and Y.-J. Zhang, "A 2.5-D angularly stable frequency selective surface using via-based structure for 5G EMI shielding," *IEEE Trans. Electromagn. Compat.*, vol. 60, no. 3, pp. 768–775, Jun. 2018.

[17] Z. Sun, B. Peng, F. Huang, Y. Yang, J. Zhu, P. He, and W. Zhang, "A miniaturized wireless passive frequency selective surface sensor for high-temperature applications," *IEEE Sensors J.*, vol. 22, no. 23, pp. 22734–22740, Dec. 2022.

[18] X. C. Tong and X. C. Tong, "Metamaterials inspired frequency selective surfaces," in *Functional Metamaterials and Metadevices*. Bolingbrook, IL, USA: Springer, 2018, pp. 155–171.

[19] P. Edenhofer and A. Alpaslan, "Active frequency selective surfaces for antenna applications electronically to control phase distribution and reflective/transmissive amplification," in *Proc. IEEE/ACES Int. Conf. Wireless Commun. Appl. Comput. Electromagn.*, Mar. 2005, pp. 237–240.

[20] M. Harnois, M. Himdi, W. Y. Yong, S. K. A. Rahim, K. Tekkouk, and N. Cheval, "An improved fabrication technique for the 3-D frequency selective surface based on water transfer printing technology," *Sci. Rep.*, vol. 10, no. 1, p. 1714, Feb. 2020.

[21] J. Li, J. Jiang, Y. He, W. Xu, M. Chen, L. Miao, and S. Bie, "Design of a tunable low-frequency and broadband radar absorber based on active frequency selective surface," *IEEE Antennas Wireless Propag. Lett.*, vol. 15, pp. 774–777, 2016.

[22] A. H. Abdelrahman, A. Z. Elsherbeni, and F. Yang, "Transmission phase limit of multilayer frequency-selective surfaces for transmitarray designs," *IEEE Trans. Antennas Propag.*, vol. 62, no. 2, pp. 690–697, Feb. 2014.

[23] Y. Hei, M. Wang, W. Wu, and Y. Wu, "A Fabry–Pérot cavity antenna with non-uniform superstrate and EBG ground for high gain and high aperture efficiency," *IEEE Access*, vol. 9, pp. 101239–101245, 2021.

[24] C. A. Balanis, *Antenna Theory: Analysis and Design*. Hoboken, NJ, USA: Wiley, 2016.

[25] D. M. Pozar, *Microwave Engineering*. Hoboken, NJ, USA: Wiley, 2011.

[26] C. A. Balanis, *Advanced Engineering Electromagnetics*. Hoboken, NJ, USA: Wiley, 2012.

[27] G. Goussetis, A. P. Feresidis, A. B. Yakovlev, and C. R. Simovski, "High-impedance surfaces," in *Theory and Phenomena of Metamaterials*. London, U.K.: Taylor & Francis, 2017, pp. 1–31.

[28] H. Mosallaei and K. Sarabandi, "Antenna miniaturization and bandwidth enhancement using a reactive impedance substrate," *IEEE Trans. Antennas Propag.*, vol. 52, no. 9, pp. 2403–2414, Sep. 2004.

[29] B. Majumder, K. Kandasamy, and K. P. Ray, "A zero index based meta-lens loaded wideband directive antenna combined with reactive impedance surface," *IEEE Access*, vol. 6, pp. 28746–28754, 2018.

[30] S. Guthi and V. Damera, "High gain and wideband circularly polarized S-shaped patch antenna with reactive impedance surface and frequency-selective surface configuration for Wi-Fi and Wi-max applications," *Int. J. RF Microw. Comput.-Aided Eng.*, vol. 31, no. 11, Nov. 2021, Art. no. e22865.

[31] T. M. Wong, K. M. Luk, and K. F. Tong, "Miniaturized via-free magneto-electric dipole antenna fed by substrate integrated coaxial line on reactive impedance surface," *IEEE Trans. Antennas Propag.*, vol. 71, no. 10, pp. 7704–7714, Oct. 2023.

[32] P. C. Bybi, G. Augustin, B. Jitha, C. K. Aanandan, K. Vasudevan, and P. Mohanan, "A quasi-omnidirectional antenna for modern wireless communication gadgets," *IEEE Antennas Wireless Propag. Lett.*, vol. 7, pp. 505–508, 2008.

[33] S. Choudhury, A. Mohan, and D. Guha, "Wideband quasi-omnidirectional planar inverted F-antenna for compact wireless systems," *IEEE Antennas Wireless Propag. Lett.*, vol. 17, no. 7, pp. 1305–1308, Jul. 2018.

[34] N. O. Parchin, M. Shen, and G. F. Pedersen, "UWB MM-wave antenna array with quasi omnidirectional beams for 5G handheld devices," in *Proc. IEEE Int. Conf. Ubiquitous Wireless Broadband (ICUWB)*, Oct. 2016, pp. 1–4.

[35] P. Wang, J. Liu, G. Huang, Q. Wu, C. Zhou, and W. Wang, "Wideband gain enhancement of high-isolation and quasi-omnidirectional metamaterial MIMO antenna for vehicular radar," *IEEE Trans. Instrum. Meas.*, vol. 71, pp. 1–12, 2022.

[36] S. Kamal, M. F. B. Ain, U. Ullah, A. S. B. Mohammed, F. Najmi, R. Hussin, Z. A. Ahmad, M. F. B. Mohamed Omar, M. F. A. Rahman, M. N. Mahmud, and M. Othman, "Wheel-shaped miniature assembly of circularly polarized wideband microstrip antenna for 5G mmWave terminals," *Alexandria Eng. J.*, vol. 60, no. 2, pp. 2457–2470, Apr. 2021.

[37] T. Yang, W. Davis, W. Stutzman, and M.-C. Huynh, "Cellular-phone and hearing-aid interaction: An antenna solution," *IEEE Antennas Propag. Mag.*, vol. 50, no. 3, pp. 51–65, Jun. 2008.

[38] *Safety Levels With Respect to Human Exposure to Radio Frequency Electromagnetic Fields, 300 kHz to 100 GHz*, Amer. Nat. Standards Inst., Washington, DC, USA, 1982.

[39] *Limitation of Exposure of the General Public to Electromagnetic Fields (0 Hz to 300 GHz)*, Off. J. Eur. Communities, IEEE, New York, NY, USA, 1999.

[40] P. Vasenkari, D. Brunel, and L. Noël, "5G RF design challenges," in *5G Technology: 3GPP New Radio*. Hoboken, NJ, USA: Wiley, 2020, pp. 349–397.

[41] Samsung-Electronics. (2019). *SMG977U (Galaxy S10 Variant) Portable Handset RF Exposure Info Near Field Power Density Simulation Report*. FCC ID: A3LSMG977U. [Online]. Available: https://fccid.io/A3LSMG977U/RF-Exposure-Info/Near-Field-Power-Density-Simulation-Report-4235748#download

[42] U. Ullah, I. B. Mabrouk, and S. Koziel, "Enhanced-performance circularly polarized MIMO antenna with polarization/pattern diversity," *IEEE Access*, vol. 8, pp. 11887–11895, 2020.

[43] K.-Y. Liu, G.-M. Wang, T. Cai, H.-P. Li, and T.-Y. Li, "Conformal polarization conversion metasurface for omni-directional circular polarization antenna application," *IEEE Trans. Antennas Propag.*, vol. 69, no. 6, pp. 3349–3358, Jun. 2021.

[44] T. K. T. Nguyen, T. M. Nguyen, H. Q. Nguyen, T. N. Cao, D. T. Le, X. K. Bui, S. T. Bui, C. L. Truong, D. L. Vu, and T. Q. H. Nguyen, "Simple design of efficient broadband multifunctional polarization converter for X-band applications," *Sci. Rep.*, vol. 11, no. 1, p. 2032, Jan. 2021.

[45] A. Kumar, G. Saxena, P. Kumar, Y. K. Awasthi, P. Jain, S. S. Singhwal, and P. Ranjan, "Quad-band circularly polarized super-wideband mimo antenna for wireless applications," *Int. J. RF Microw. Comput.-Aided Eng.*, vol. 32, no. 6, p. e23129, 2022.

[46] M. K. Khandelwal, S. Kumar, and B. K. Kanaujia, "Design, modeling and analysis of dual-feed defected ground microstrip patch antenna with wide axial ratio bandwidth," *J. Comput. Electron.*, vol. 17, no. 3, pp. 1019–1028, Sep. 2018.

[47] R. Dhara, "A compact dual band dual polarized monopole antenna with enhanced bandwidth for C, X, and Ku band applications," *Prog. Electromagn. Res. Lett.*, vol. 96, pp. 65–72, 2021.

[48] K. Katoch, N. Jaglan, and S. D. Gupta, "Design and analysis of single sided modified square loop UWB frequency selective surface," *IEEE Trans. Electromagn. Compat.*, vol. 63, no. 5, pp. 1423–1432, Oct. 2021.

[49] K. Katoch, N. Jaglan, S. D. Gupta, and M. S. Sharawi, "Design of a triple band notched polarization independent compact FSS at UWB frequency range," *Int. J. RF Microw. Comput.-Aided Eng.*, vol. 31, no. 6, Jun. 2021, Art. no. e22631.

[50] K. Katoch, N. Jaglan, and S. D. Gupta, "Analysis and design of a simple and compact bandstop frequency selective surface at mobile WiMAX and satellite communication X-band," *J. Electromagn. Waves Appl.*, vol. 35, no. 10, pp. 1321–1336, 2021.

SHAHANAWAZ KAMAL was born in Mumbai, India, in 1991. He received the Diploma in electronics and telecommunication engineering from the Maharashtra State Board of Technical Education, India, in 2010, the B.E. and M.E. degrees in electronics and telecommunication engineering from the University of Mumbai, India, in 2013 and 2017, respectively, and the Ph.D. degree in antenna and propagation from Universiti Sains Malaysia, Malaysia, in 2022. He was an In-Building Solution Engineer at Vedang Cellular Services, India, in 2014. He was a Visiting Lecturer with MH Saboo Siddik Polytechnic, India, in 2016. He was affiliated as a Graduate Research Assistant with Universiti Sains Malaysia, from 2019 to 2022. He is currently a Senior Researcher with Barkhausen Institut, Germany. He has published several technical papers in refereed journals, books, and conference proceedings.

His current research interests include conceptualization, design, development, and measurement of RF circuits, on-chip MIMO antennas, and metasurfaces for the IoT over satellite, joint communications and sensing, monostatic radars, and 6G applications. He regularly serves as a Peer Reviewer for the *Journal of Electromagnetic Engineering and Science*, *Progress in Electromagnetics Research*, *International Journal of RF and Microwave Computer-Aided Engineering*, *Electronics Letters*, and IEEE Access.

PADMANAVA SEN (Senior Member, IEEE) received the B.Tech. degree in electronics and electrical communication engineering from the Indian Institute of Technology, Kharagpur, India, in 2003, and the M.S. and Ph.D. degrees from the Georgia Institute of Technology, Atlanta, GA, USA, in 2005 and 2007, respectively. In 2010, he joined Broadcom Corporation, Irvine, CA, USA, where he worked towards the development of phased array systems at 60GHz frequency bands (802.11ad), for six years. Apart from Broadcom Corporation (Irvine and Bangalore, India), he worked at Sayana Wireless, Atlanta, a 60 GHz startup, for three years, and at IBM Corporation, Vermont, USA, for one year. In 2018, he joined Barkhausen Institut, Dresden, Germany. He is currently leading the RF Design Enablement Group, Barkhausen Institut, with a focus on joint communications and sensing. He has authored or coauthored over 50 IEEE journals and conference papers. He holds three issued U.S. patents.

● ● ●